Journal of Electron Spectroscopy and Related Phenomena 265 (2023) 147334

Contents lists available at ScienceDirect

Journal of Electron Spectroscopy and Related Phenomena

journal homepage: www.elsevier.com/locate/elspec

Scanning transmission X-ray spectromicroscopy: A nanotool to probe hematite nanorods for solar water splitting

Stefan Stanescu [a,*], Dana Stanescu [b], Adam Hitchcock [c]

[a] Synchrotron SOLEIL, L'Orme des Merisiers, Départementale 128, 91190 Saint-Aubin, France
[b] SPEC, CEA, CNRS, Université Paris-Saclay, CEA Saclay, 91191 Gif-sur-Yvette Cedex, France
[c] Department of Chemistry & Chemical Biology, McMaster University, Hamilton, ON L8S 4M1, Canada

ARTICLE INFO

Keywords:
Hematite
Photoanode
Water splitting
STXM
Spectromicroscopy

ABSTRACT

We report a scanning transmission X-ray microscopy (STXM) study of hematite nanorods, prototypical photoanode used in solar water splitting. Hematite nanorods were obtained by hydrothermal growth from aqueous solutions using $FeCl_3$ as precursor. Potentials for onset of water splitting are smaller using this synthesis method, compared to values reported for hematite photoanodes obtained by epitaxial growth. STXM revealed the presence of a hexahydrate iron chloride phase at the surface of the nanorods, which is linked to the low onset potential values. We detail the quantification approach that revealed the specific microstructure of individual hematite nanorods.

1. Introduction

Clean and sustainable energy production and storage is the major challenge for mankind today [1–4]. Although clean energy can be produced economically from aeolian, hydro, solar, *etc.*, only a minor part is stored, since as yet, there is no perfect energy storage technology [5]. Hydrogen offers a viable approach with a large storage capacity of 142 MJ/kg. At present, more than 95% of the hydrogen produced is obtained by steam methane reforming. Although this is the most efficient technology known at present (> 70% efficiency [6]), this way of producing hydrogen is far from being clean or sustainable, since for every ton of hydrogen produced, 2–9 tons of CO_2 are emitted depending on the details of the process. Water dissociation into H_2 and O_2 through electrolysis, offers an alternative for hydrogen production, particularly when using electricity from renewable sources. An important amount of external electrical energy input is mandatory to overcome the water redox potential of 1.23 V (1.6 V if we consider overpotentials at the electrodes). As an example, an industrial electrolyser producing 750 Nm^3/h consumes an electrical energy of approx. 5 kWh for each Nm^3 of H_2 produced [7]. Since 1972, when Fujishima and Honda [8] first proposed the concept of using photosensitive anodes, like TiO_2, in dedicated photoelectrochemical (PEC) cells to split water, a major research effort has been devoted to optimizing semiconductor photoelectrodes, to match a list of needed properties regarding: i) light absorption, ii) surface kinetics during electrochemical reactions, iii) charge separation and bulk electrical conduction, iv) chemical composition and stability, *etc.* [9–13]. Since common materials do not meet all requirements, band engineering is explored intensively to overcome intrinsic materials drawbacks. The principal target for these studies is achieving the maximum generated photocurrent for the minimum energy input. Thus, the onset potential, related to the energy input necessary to initiate the solar water splitting (SWS) reaction, represents one of the key parameters used to evaluate the PEC activity. In this respect the aim is to find ways to modify both the bulk and surface of the semiconductor, which decrease the onset potential. Approaches include surface activation by specific catalysts [14–16], partial surface etching [17], band engineering by doping, annealing or hetero-structuring [18–20].

Hematite is the prototypical semiconducting material used as a SWS photoanode. It is characterized by a band gap of 2.15 eV, which perfectly matches the solar spectrum for optimized absorption, which is ideal for direct SWS [13]. Compared to materials exhibiting higher photocurrents (*e.g.* $BiVO_4$) [21], pristine hematite is less efficient for SWS mainly because of the reduced hole mean free path (~ 2–4 nm) and poor surface kinetics, mainly due to a complex oxygen evolution reaction (OER) mechanism [18]. Therefore, the photocurrents obtained using pristine hematite as photoanode are much lower (in μA range) than the expected value of 12.6 mA/cm^2, calculated assuming 100% collection and conversion of the photogenerated electron-hole pairs to electronic current

* Corresponding author.
E-mail address: stefan.stanescu@synchrotron-soleil.fr (S. Stanescu).

https://doi.org/10.1016/j.elspec.2023.147334
Received 12 March 2023; Received in revised form 8 May 2023; Accepted 8 May 2023
Available online 9 May 2023

[22]. Nevertheless, its abundance, chemical stability under alkaline conditions, and low environment impact prevail upon other considerations to keep hematite on the list of materials being actively studied for possible SWS applications.

There are two main categories of synthesis methods used for semiconducting oxide photoanodes. The first category corresponds to "model" samples, continuous and homogenous, allowing control and hence study of each photoanode parameter individually (*e.g.* crystalline structure, thickness, chemical stoichiometry, doping level, *etc.*). Atomic oxygen assisted molecular beam epitaxy (AO-MBE) [17,20], magnetron sputtering [23], pulsed layer deposition [24,25], and atomic layer deposition [26,27], are among the synthesis methods used to make "model" samples. The second category targets fabrication of nanostructured / self-assembled architectures (such as nano-wires or nano-rods, column-like porous architectures, core-shell structures, *etc.*) where the layers are heterogeneous in terms of morphology, crystallography, and electronic, or chemical structure. For that type of samples, one can use spin-coating [28,29], aqueous chemical growth (ACG) [10,30], hydrothermal electrochemical deposition [31], sol-gel [32]. These methods are more versatile in terms of ease of setup and variability of growth parameters allowing the deposition of high-quality oxide nanostructures, uniformly grown on larger surfaces, characteristics which are more pertinent for technological implementation in future SWS applications.

It is often difficult to directly compare photocurrent values reported in the literature, since very often different measurement protocols are used (*e.g.* stabilized *vs.* dynamic measurements as detailed in [10]), and no standardization is applied for electrolyte type – NaOH, KOH; acidity – molarity – 0.1 M, 1 M, 3 M; and power of solar simulator used, *etc.* Here we compare hematite-based photoanodes prepared and measured in the same laboratory, using strictly the same setup and similar conditions (electrolyte and solar simulator). Within these conditions, we observe lower photocurrent values, higher transients, and higher onset values for the "model" photoanodes, obtained by AO-MBE epitaxial growth [17,20], compared to those obtained by the ACG synthesis method [10].

Scanning transmission X-ray microscopy (STXM) was established as a powerful technique in the late 1980s by pioneering work by the Stony Brook university group at NSLS-1 [33,34]. Its capacity for discriminating fine chemistry and chemical coordination variations at nanoscale, distinguish STXM as a tool of choice for materials characterization [35,36]. STXM uses Near-Edge X-ray Absorption Fine Structure (NEXAFS) spectroscopy [37] as its main contrast mechanism, which provides speciation and electronic structure information from heterogeneous, nanostructured samples. NEXAFS microscopy using a STXM is a particularly powerful tool for studies of the 3d transition metal oxides important in SWS [38].

We report here a STXM study of the origin of the reduced onset potential determined from PEC measurements of nanorod hematite photoanodes synthesized by hydrothermal growth from aqueous solutions (ACG). STXM spectromicroscopy successfully quantified the chemical composition of the heterogeneous hematite nanorods and determined the nature of the hematite photoanode/electrolyte interface. A proton-rich phase at the photoanode/electrolyte interface was detected by STXM. This surface phase decreases the potential needed for photocurrent generation, *i.e.* the onset potential for the water splitting process.

2. Results and discussion

The ACG synthesis method offers an easy, cheap, and versatile way of obtaining nanostructured photoanodes [10,30]. Guided by a global low environmental impact approach, samples were synthesized from $FeCl_3$ salt dissolved in water, with pH values controlled by adjusting the salt quantity. No additives were used to control solution pH value or growth rate. Nanostructured hematite layers prepared by the ACG method were deposited on Fluorine-doped Tin-Oxide (FTO) coated glass substrates. Thus, hydrothermal activation at 95 °C for several hours was used to generate the β-FeOOH phase (akaganeite). Air annealing at 500 °C is employed in a second step to induce a phase transformation of β-FeOOH to hematite, α-Fe_2O_3. As reported in the literature for the ACG method [39], a strict protocol for the cleaning of the FTO substrates must be followed to get uniformly grown layers and thus reproducible PEC measurements. The detailed protocol used to prepare the samples studied in this work was reported in a previous publication [10]. We remind here briefly that several growth parameters play an important role in determining the resulting morphology, especially regarding the length of nanorods, while their width remains constant. Thus, varying the deposition time from 4 to 24 h, allow tuning the length of the nanorods, at fixed pH value. As an example, at pH = 1.4, we can vary the nanorods length from ~200–500 nm. This variation is limited though, and we observed that nanorods appear quite rapidly during the hydrothermal process. The samples we used in the present study were all grown for 24 h. Nanostructured hematite films are thus obtained, composed of nanorods oriented perpendicularly to the substrate in a carpet or brush-like morphology (Fig. 1). It is worth mentioning here, without diving into details beyond the purpose of this report, that diffraction measurements showed the nanorods had the [110] hematite crystallographic axis orientation perpendicular to the FTO substrate. The [110] orientation in hematite is the electrical conduction easy axis and is thus beneficial to PEC applications. In addition, X-ray diffraction data collected using in-plane geometry, showed a powder like diffraction pattern, implying a fully isotropic (*i.e.* non-textured) in plane orientation of the hematite nanorods [10]. Tuning the pH value leads to a variation of the nanorod length, from ~1 μm to ~300 nm in pH ranges from 1.0 to 1.4, respectively. Figs. 1a–c are Scanning Electron Microscopy (SEM) images of samples grown in solutions with pH = 1.0, 1.2 and 1.4 respectively. In all cases uniform brush-like layer of hematite nanorods grow perpendicularly to the surface of the FTO substrates. By increasing the pH of the solution from 1.0 to 1.4, the number of irregularly oriented nanorods grown as overlayer is reduced. While the nanorod length varies when varying the pH value, their width (50–100 nm) remains relatively constant. An SEM image of a cross-section of the hematite "brush" fabricated by ultramicrotomy (Fig. 1g), clearly shows the ~80 nm thick, bright, FTO substrate layer and the well-defined hematite nanorods. Air-annealing at 500 °C, typically applied to transform the akaganeite to hematite phase, doesn't seem to visibly affect the morphology of the nanorods. We expected morphological changes during the phase transition from akaganeite to hematite since there should be mass reduction from water and chlorine loss with increasing temperature.

PEC activity is characterized for all samples by photocurrent measurements. For this purpose, fast sweep (50 mV/sec) voltammetry is performed using a dedicated setup detailed elsewhere [10]. Fig. 2 presents the photocurrent densities, J_{ph}, as a function of the applied potential V (*vs.* RHE) obtained from the ACG synthesized sample, in comparison with an epitaxial counterpart [40]. All hematite photoanodes give low photocurrent density values, well below 1 mA/cm^2. Miao et al. [41] show that by increasing the open-circuit PEC voltage ($\Delta V_{F,OC}$), defined as the difference between the Fermi levels for electrons (E_{Fn}) and holes (E_{Fp}) upon illumination, the onset potential and, therefore, the input energy necessary to initiate the OER, decreases. Iandolo et al. [42], have shown that: i) complex charge transfer processes that occur during OER, which are dominated by the presence of surface states at the photoanode/electrolyte interface; and ii) small photovoltages, are the main factors responsible for the onset potential increase with respect to the ideal hematite photoanode, for which the onset potential is estimated to be between 0.4 and 0.6 V *vs.* RHE. The onset potential values for the hematite nanorods obtained by ACG, are lower compared with those for model hematite photoanodes obtained by AO-MBE, where metallic Fe is deposited in oxidizing conditions in a strictly controlled ultra-high vacuum environment. Photoanodes obtained by ACG show an onset potential lower than + 0.6 V *vs.* RHE [10], while those obtained by AO-MBE exhibit values ≥ 1.0 V *vs.* RHE [17,

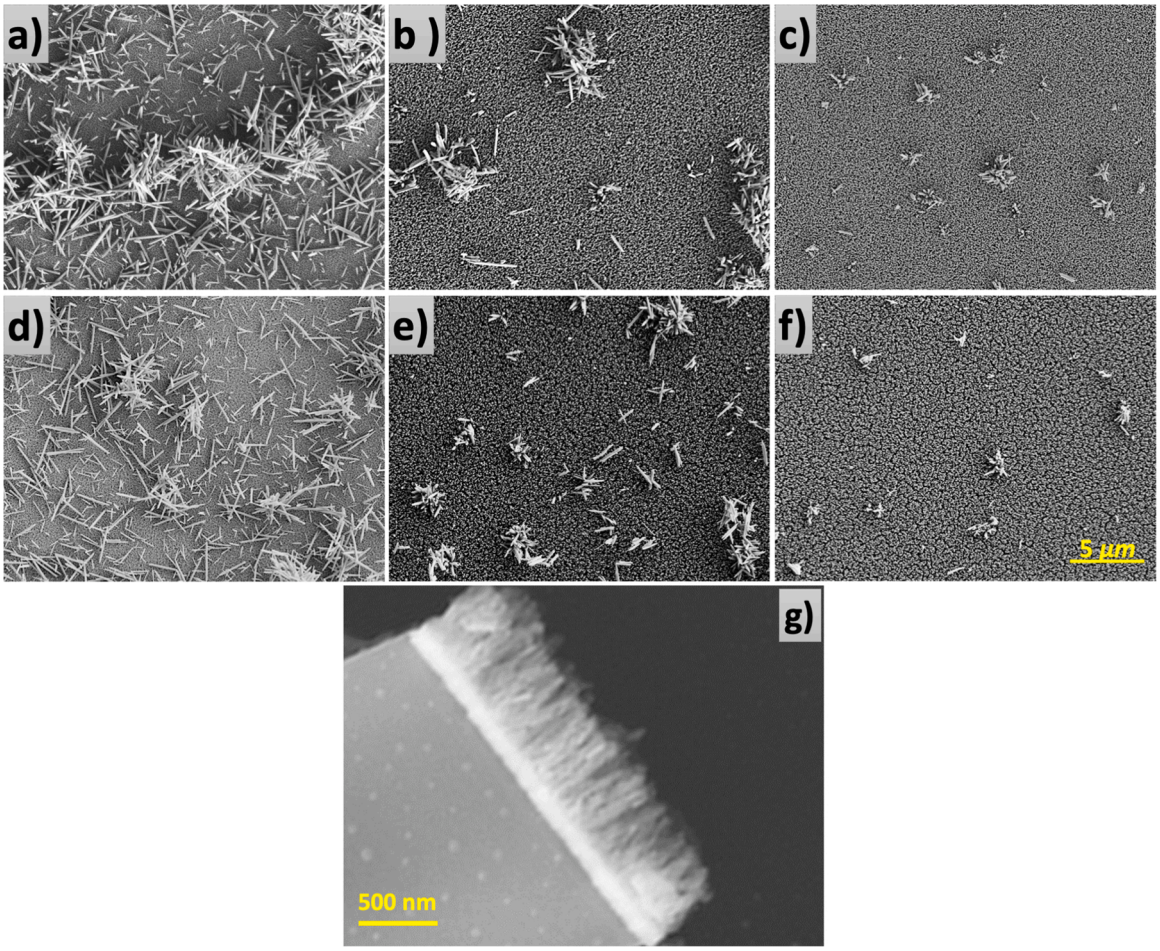

Fig. 1. Overview of SEM images measured from the samples grown in solutions with pH = 1.0 (a and d), 1.2 (b and e), and 1.4 (c and f), in akaganeite phase (1st row) and hematite phase (2nd row). We remark the same uniform underlayer composed of nanorods pointing out from the surface for all pH values. Decreasing the pH value increases the number of the irregularly oriented nanorods growing on the top of the well-defined, carpet-like hematite layer. g) ultramicrotome section through the nanostructured hematite layer, showing ~500 nm long nanorods. The bright, well-defined layer below the hematite nanorod "brush" is the FTO substrate on top of very thick glass support.

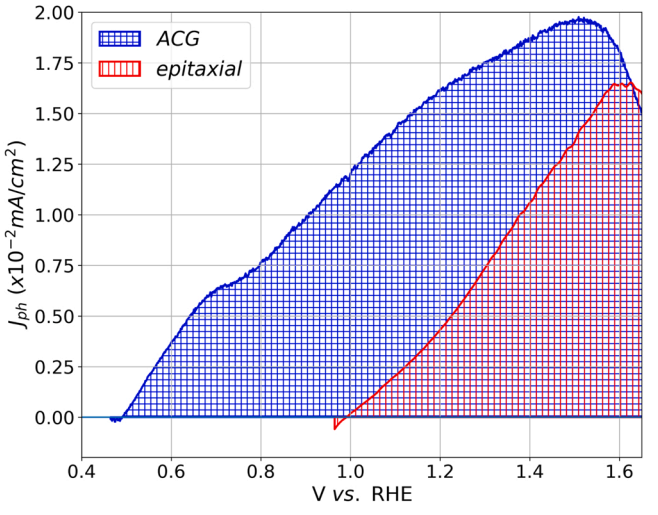

Fig. 2. photocurrent density measured for epitaxial (red) and synthesized by ACG (blue) hematite samples.
Data for epitaxial sample adapted from [40]

20]. At first sight, morphology accounts for this difference. Indeed, the photoanode surface exposed to the electrolyte is estimated to be more than 40 times larger for the ACG deposited nanorods than AO-MBE samples. The factor of 40 is derived using a simple model: each 2500 nm^2 unit surface is assumed to be replaced by a parallelepiped with 50 × 50 nm^2 base and 500 nm height. Nevertheless, the increase of the size of the active interface should lead to a proportional increase of the photocurrent. When comparing the two kinds of samples, an increase of the photocurrent value is observed, but not proportional to the increase in surface area. Charge transfer at the semiconductor/electrolyte interface, related to a specific chemistry, might account for the onset potential differences. To test this hypothesis, we studied the ACG hematite nanorods using the STXM at the HERMES beamline [43] of the SOLEIL synchrotron facility.

For this study the STXM was equipped with a 30 nm last zone width Fresnel zone plate (FZP) giving ~40 nm spot size at the sample. A 50 µm diameter OSA (Order Sorting Aperture) used in conjunction with the 80 µm FZP' beam-stop removed zero order (*i.e.* transmitted, undiffracted X-rays) and higher diffraction orders. STXM was operated mainly by recording hyperspectral data (energy stacks), tuning the energy of the incoming photons from 450 to 850 eV, covering the O K and Fe $L_{2,3}$ absorption edges. It is important to mention that energy stacks were measured by recording the whole energy range (from 450 to 850 eV) at once, making possible direct comparison with the calculated linear mass absorption coefficients from the atomic scattering factors

[44]. Thus, chemical composition can be determined in terms of elemental ratio, *i.e.* O:Fe. To start we measured commercial 50 nm pure hematite nano-powder from Sigma-Aldrich. The sample was prepared by drop casting 1 μL from a suspension of hematite particles in mixed 1:1 isopropanol – pure water onto a 50 nm thickness SiN membrane. Fig. 3a presents the spectrum recorded from one isolated hematite particle. We used aXis2000 software [45] to analyze the STXM data. Despite the noise present in the data recorded from a single < 50 nm nanoparticle, we can compare it to the corresponding atomic continuum using the optical density expression $OD = \mu(E) \cdot d$, with $\mu(E)$ the energy dependent linear attenuation coefficient and d the thickness of the nanoparticle. The linear attenuation coefficient varies as a function of the X-ray wavelength, λ, following the relationship $\mu(E) = 4\pi\beta/\lambda$, where $\beta = r_0\lambda^2 f_2 n_{at}/2\pi$ is the imaginary part of the index of refraction, $n = 1 - \delta - i\beta$, with r_0 the classical electron radius, n_{at} the atomic number density, and f_2 the absorptive part of the X-ray scattering factor. The calculated linear attenuation coefficient using the stoichiometric 3:2 O:Fe ratio for hematite, does not reproduce the experimental data (blue solid line in Fig. 3a). This may arise from uncertainties of the atomic scattering factors at the L-edges. To reach an O:Fe ratio able to reproduce our data (solid red line in Fig. 3a), we need to increase the O:Fe ratio. To this purpose we introduce hexahydrate iron chloride ($FeCl_3{\cdot}6\ H_2O$) (*hexa*) as a component of the linear combination with hematite (*hema*), $c \times hema + (1 - c) \times hexa$, and fit the experimental data leaving the hematite proportion as free parameter. The best fit was obtained with only 42% hematite and 58% $FeCl_3{\cdot}6\ H_2O$. It is interesting to note that the extracted thickness after the fitting procedure is closer to the expected value, due to the lower density of $FeCl_3{\cdot}6\ H_2O$ (1.82 g/cm^3) compared to hematite (5.3 g/cm^3). Considering the synthesis of our samples, which used $FeCl_3$ in aqueous solution, we choose $FeCl_3{\cdot}6\ H_2O$ to introduce a higher O:Fe ratio. We proceed in a similar way using a sample obtained by drop casting 1 μL of $FeCl_3$ from an aqueous solution with pH = 1. The result is presented in Fig. 3b. Again, using theoretical values for $FeCl_3{\cdot}6\ H_2O$, we cannot fit the experimental data, but this time the calculated atomic continuum underestimates experimental data. By introducing Fe_2O_3 in a linear combination with $FeCl_3{\cdot}6\ H_2O$, we can perfectly fit the data using an 18% hematite content. Assuming that the commercial hematite and hexahydrate iron chloride are 100% pure, we can extract a composition rescaling formula as $c = (c_{fit} - c_{hexa})/(c_{hema} - c_{hexa})$, where c is the final estimated hematite content, c_{fit} the hematite content extracted from the fit using the linear combination of Fe_2O_3 and $FeCl_3{\cdot}6\ H_2O$, $c_{hexa} = 0.18$ the hematite content extracted for the $FeCl_3{\cdot}6\ H_2O$ reference sample, and $c_{hema} = 0.42$ the hematite content extracted from the Fe_2O_3 sample.

We used these reference measurements and the composition rescaling formula to check the chemical composition of individual hematite

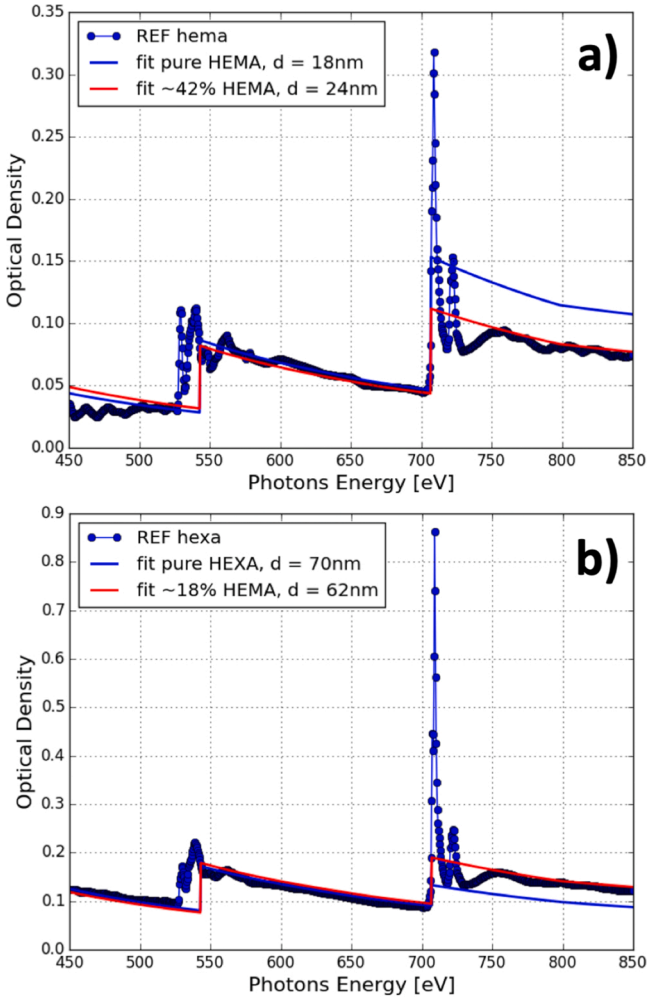

Fig. 3. NEXAFS reference spectra recorded from the hematite (a) and hexahydrate iron chloride (b) samples. The experimental data (blue circles) were reproduced using a linear combination of calculated hematite and hexahydrate iron chloride using the respective atomic scattering factors. We remark that theoretical chemical composition for each of the compounds does not reproduce the experimental data.

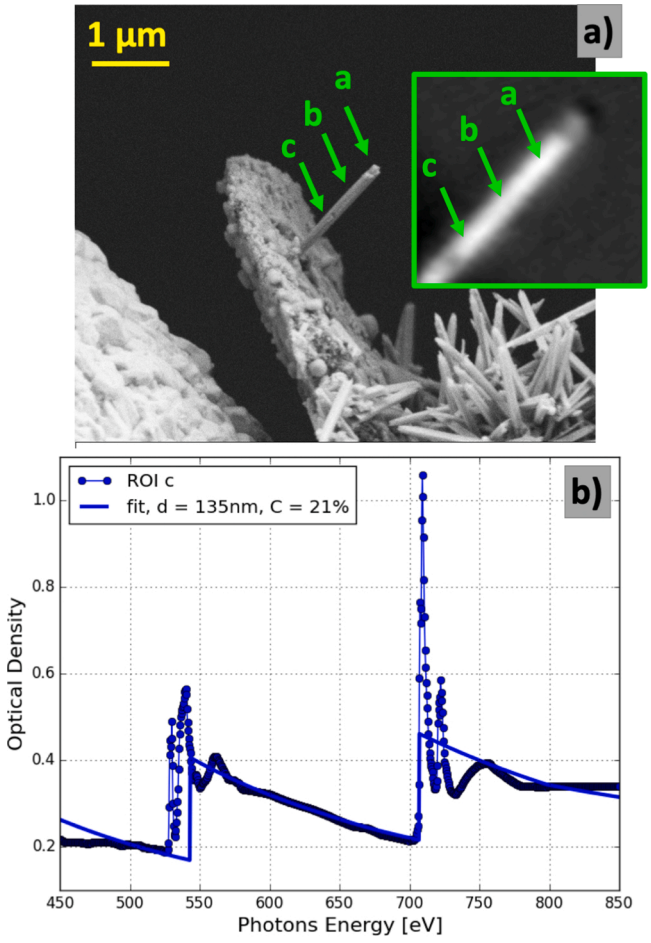

Fig. 4. Chemical composition along a single hematite nanorod. a) SEM image used to isolate the useful measurement regions for STXM; (inset) image at the Fe L_3 absorption edge (711 eV) showing the 3 regions from where spectra were extracted to determine chemical composition. Three ROIs are indicated as *a*, *b*, and *c* that were selected to extract the chemical composition values detailed in the text; b) NEXAFS spectrum extracted from the region marked with *c*.

nanorods obtained by ACG from an aqueous solution with pH = 1 and then annealed at 500 °C in air. Fig. 4**a** presents results from a single hematite nanorod isolated with the help of SEM prior to the STXM measurements. This sample was obtained by scraping the hematite sample deposited on the FTO substrate and then transferring the material to a standard TEM (Transmission Electron Microscopy) copper grid. The scraping method preserves morphology integrity for the hematite layers transferred on the TEM grid. In this way we could isolate several regions with individual hematite nanorods, protruding from the FTO / "brush" layer, like the one shown. in Fig. 4a. This SEM image was obtained using secondary electron detection at relatively low acceleration voltage (3 kV). In this manner mainly nanorod topography is probed. The inset show a 1 μm^2 STXM scanned area where the hematite nanorod gives very good contrast OD ~ 1 at the Fe L_3 absorption edge. We compared 3 regions marked with *a*, *b*, and *c* respectively, to extract the relative hematite composition applying the approach described above. As an example, Fig. 4b shows the spectrum from region *c*. The hematite content corresponds to 21% hematite in the 135 nm thick nanorod. Regions *a* and *b* were found to have 25% and 31% hematite, with 117 and 135 nm thickness, respectively. Aside from the hematite content being very low, possibly somehow underestimated within this approach, it is clear that the nanorod is chemically heterogeneous. There are indeed contrast variations in the STXM image shown in Fig. 4a inset, but this direct imaging approach fails in extracting more valuable information. It is worth mentioning here, without further details, that we didn't succeed in getting more information using the PCA (Principal Component Analysis) – cluster analysis as implemented in MANTIS (Multivariate ANalysis Tool for Spectromicroscopy) software [46]. Indeed, we observe the same compositional variations along the nanorod, without evidence of spatial distribution or spectral identification.

To quantify hematite nanorod' chemistry, we used the spectra in Fig. 3 as references and convert them into OD1 units, *i.e.* OD per 1 nm of material at its standard density [35]. To this purpose we used the best fits of the atomic continuum (red solid curves in Fig. 3) and then normalized the experimental spectra to the extracted thickness. Density values of 5.3 g/cm^3 for hematite, and 1.82 g/cm^3 for hexahydrate iron chloride were used. Thus, the spectrum in OD1 units for hematite was obtained by dividing the experimental spectrum by 24, while the OD1 spectrum of hexahydrate iron chloride one was obtained by dividing the experimental spectrum by 62. We then applied the SVD (Singular Value Decomposition) method implemented in aXis2000 to the STXM hyperspectral data using these reference spectra to obtain a quantitative chemical mapping, *i.e.* spatial distribution of the two spectral components. Fig. 5 shows the result of the SVD with the two main components being the spatial regions which match the reference spectra, using red for hematite and green for the hexahydrate iron chloride. An additional contribution was identified as arising from carbon contamination due to the several measurements we had to perform to get a dataset with good statistics. To quantify the carbon component, we performed an energy stack across the C K-edge absorption edge, from 270 to 320 eV. The inset in Fig. 5 shows the difference between images recorded post- (320 eV) and pre- (270 eV) C K-edge. The C K-edge contrast in this difference image (a carbon map) is due to the X-ray induced carbon layer deposition on the nanorod. Since we use OD1 units reference spectra, the RGB mapping is quantified in terms of the thickness, *i.e.* nm units, and thus the color-bar scale is given in nm units and the color intensity of each component in the map indicates the thickness of that component. Hematite has a maximum intensity of 105 nm in the left center of the core of the nanorod, while hexahydrate iron chloride has a maximum intensity of 51 nm at the interface of the nanorod and the FTO support layer. To calculate the deposited carbon contribution, the SVD was determined in OD units and then converted to thickness using the elemental response for pure C and a density of 2 g/cm^3 density (amorphous carbon). The extracted maximum value for carbon in the map is 85 nm, a value that corresponds to the size of the sides of the nanorod. Comparing this value to the expected width of the nanorods of ~100 nm as determined from SEM, most probably the C layer is a few nanometers thick with a density that is < 2 g/cm^3. In this color-coded composite image the astonishing 650 nm long and 110 nm wide hematite nanocrystal with well-defined rectangular shape, is seen clearly. At both ends, the hexahydrate iron chloride phase is present in larger quantity,

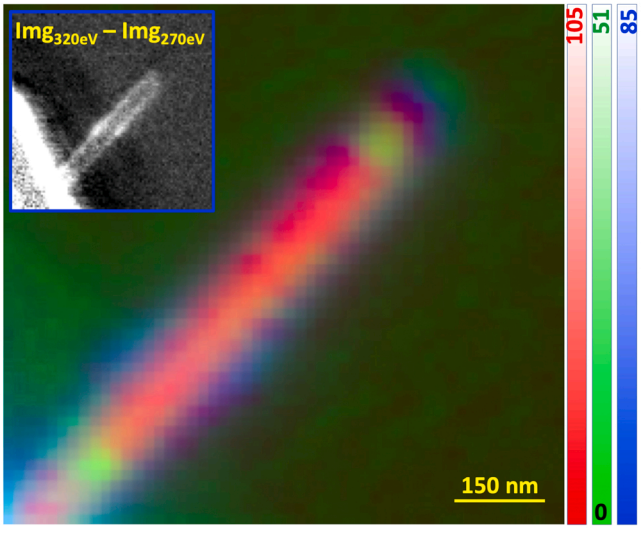

Fig. 5. RGB chemical mapping using reference OD1 spectra for hematite (Red), hexahydrate iron chloride (Green), and carbon (Blue). Color bars are given in nm units. Inset presents the chemical contrast obtained as the difference between the STXM images recorded before C absorption edge (270 eV) and after (320 eV), evidencing the carbon contamination accumulated over several measurements.

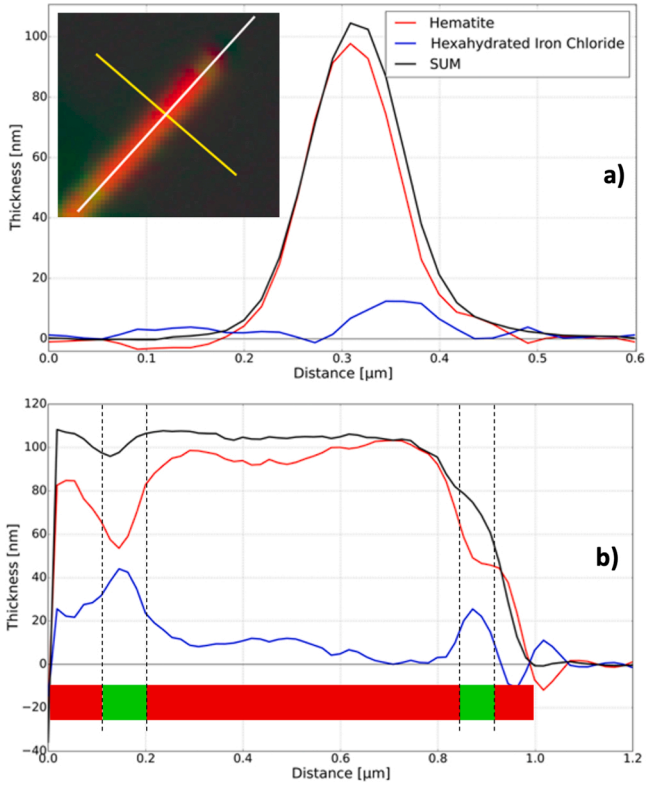

Fig. 6. Transverse (a) and longitudinal (b) crosscuts through the nanorod. Red line corresponds to hematite, blue to hexahydrate iron chloride phase, respectively, and black is the sum of the contributions, equivalent to the topographic crosscut.

characterized by a visibly brighter green component. Fig. 6 presents crosscuts along (Fig. 6b) and transverse (Fig. 6a) to the nanorod, as indicated in the inset to Fig. 6. The spatial distribution of the two iron phases is remarkably defined. Indeed, the hematite nanocrystal is only partially surrounded by the hexahydrate iron chloride. Rather the $FeCl_3 0.6\ H_2O$ is more prominent at the right side of the nanorod. Along the nanorod, the distribution of the iron phases vary, with increased hematite content toward the tip of the nanorod, while $FeCl_3 0.6\ H_2O$ phase increases toward the FTO substrate, such that the overall thickness remains constant at ~110 nm. A schematic of the morphology is presented at the bottom of Fig. 6b. The results clearly show that the 650 nm long hematite single nanocrystal is surrounded by hexahydrate iron chloride rich regions. The overall (sum) thickness values for the nanorod matches perfectly the values extracted from the SEM images in Fig. 4a.

These results reveal several interesting facts. The existence of a non-transformed hexahydrate iron oxide phase at the surface of the nanorods may explain why morphology does not change upon annealing. Annealing at 500 °C does not produce the highest photocurrent values, as previously reported [10,47]. Here we present direct evidence, using nanoscale spectromicroscopy, that at low annealing temperature the precursor phase is not fully transformed to hematite. Moreover, it is more likely that the akaganeite phase is not pure. Rather the nanorods contain iron chloride-based phases even after annealing at 500 °C. For the first time, due to using the STXM nanoprobe, a gradient of the useful hematite phase, with increased fraction toward the tip of the nanorods, is revealed. This suggests that the phase transformation does not occur homogenously along the nanorod, but rather starts from the tip. Furthermore, the segmented nanorod morphology implies that during the phase transformation hematite crystals form by an aggregation mechanism as evidenced using *in-situ* X-ray diffraction [10]. Additional useful results about the nanoscale mechanism driving the phase transformation could be obtained by *in-situ* STXM [48]. It is also interesting that, despite the initial spectral approximation (*i.e.* considering the linear combination of hematite and hexahydrate iron chloride), the SVD approach using the references in OD1 units produces thickness values that are in perfect agreement with the nanorod dimensions from SEM measurements. Finally, there are obvious implications to the PEC activity of the distribution of the specific iron phases. Even considering the "simple" case of an ideal hematite surface, the OER driving the PEC activity is a very complex process [49]. From Fig. 6 it appears that a major part of the surface exposed to the electrolyte is the hexahydrate iron chloride phase, and only a small part of the surface is hematite. We assume that $FeCl_3 0.6\ H_2O$ acts as a Brønsted Lowry acid, presenting slightly increased h^+ concentration at the interface with the electrolyte, *i.e.* acting as a proton donor. Indeed, similarly to hexa-aqua complex ions, the Fe^{3+} cations will cause the electrons to be pushed away from the O^{2-}. As a result, the electron pairs from the O-H bonds will be pulled toward the O^{2-} creating an apparent overall positive charge. Thus, during the photocurrent generation, upon increasing the external voltage, charge transfer occurs at the photoanode/electrolyte interface for lower values at the $FeCl_3 0.6\ H_2O$ surface regions, when compared to hematite. This leads to an overall lower value for the measured onset potential.

3. Conclusions

We have demonstrated the use of STXM spectromicroscopy to probe the nanoscale morphology and chemistry of hematite nanorods used as photoanodes in solar water splitting process. Two analytic approaches are presented, derived from reference spectra recorded from commercial hematite and synthesized hexahydrate iron chloride. The elemental continuum of the X-ray absorption spectra (away from the O K- and Fe $L_{2,3}$ edges) cannot be reproduced simply from the scattering factors given in the Henke tables [43] using the expected elemental composition. To achieve a good fit, we needed to use a linear combination of the experimental spectra measured from hematite and hexahydrate iron chloride. Choosing different ROIs and extracting the iron phase ratio evidenced heterogeneous chemistry along the nanorod, but with poor quantification. SVD, used as a second analytic approach, gave much more consistent and convincing results. First, to our astonishment, the chemical component map for hematite from the SVD analysis revealed with very good resolution that the hematite single nanocrystal was spatially separated in the interior of the nanorod. Second, thickness quantification mapping revealed the spatial distribution of the two iron phases, showing that the akaganeite to hematite phase transformation occurs from the tips of the nanorods. Finally, the particular morphology of the nanorods, *i.e.* exposing mostly hexahydrate iron chloride to the electrolyte, explains, through its acidic character, why the onset potential values estimated for these photoanodes were significantly lower than for the epitaxial hematite photoanodes.

Declaration of Competing Interest

The authors declare that they have no known competing financial interests or personal relationships that could have appeared to influence the work reported in this paper.

Data Availability

Data will be made available on request.

Acknowledgements

Authors thank Dris Ihiawakrim from IPCMS laboratory in Strasbourg for the ultramicrotomy cuts performed on the samples. SOLEIL facility is acknowledged for providing beamtime (project number 20170266) for this study. For the purpose of Open Access, a CC-BY public copyright license has been applied by the authors to the present document and will be applied to all subsequent versions up to the Author Accepted Manuscript arising from this submission.

References

[1] T. Abbasi, S.A. Abbasi, 'Renewable' hydrogen: prospects and challenges, Renew. Sustain. Energy Rev. 15 (2011) 3034–3040, https://doi.org/10.1016/j.rser.2011.02.026.
[2] V.M. Maestre, A. Ortiz, I. Ortiz, Challenges and prospects of renewable hydrogen-based strategies for full decarbonization of stationary power applications, Renew. Sustain. Energy Rev. 152 (2021), 111628, https://doi.org/10.1016/j.rser.2021.111628.
[3] C. Jiang, S.J.A. Moniz, A. Wang, T. Zhang, J. Tang, Photoelectrochemical devices for solar water splitting – materials and challenges, Chem. Soc. Rev. 46 (2017) 4645–4660, https://doi.org/10.1039/C6CS00306K.
[4] K. Villa, J.R. Galan-Mascaros, N. Lopez, E. Palomares, Photocatalytic water splitting: advantages and challenges, Sustain. Energy Fuels 5 (2021) 4560–4569, https://doi.org/10.1039/D1SE00808K.
[5] Z. Abdin, A. Zafaranloo, A. Rafiee, W. Merida, W. Lipinski, K.R. Khalilpour, Hydrogen as an energy vector, Renew. Sustain. Energy Rev. 120 (2020), 109620, https://doi.org/10.1016/j.rser.2019.109620.
[6] https://h2tools.org/hyarc/hydrogen-data/hydrogen-production-energy-conversion-efficiencies (accessed 12 March 2023)
[7] https://www.cea.fr/Documents/Les%20technologies%20de%20l%E2%80%99hydrog%C3%A8ne%20au%20CEA.pdf, 2012 (accessed 12 March 2023)
[8] A. Fujishima, K. Honda, Electrochemical Photolysis of Water at a Semiconductor Electrode, Nature 238 (1972) 37–38, https://doi.org/10.1038/238037a0.
[9] H.-C. Fu, P. Varadhan, C.-H. Lin, J.-H. He, Spontaneous solar water splitting with decoupling of light absorption and electrocatalysis using silicon back-buried junction, Nat. Commun. 11 (2020) 3930, https://doi.org/10.1038/s41467-020-17660-0.
[10] D. Stanescu, M. Piriyev, V. Villard, C. Mocuta, A. Besson, D. Ihiawakrim, O. Ersen, J. Leroy, S.G. Chiuzbaian, A.P. Hitchcock, S. Stanescu, Characterizing surface states in hematite nanorod photoanodes, both beneficial and detrimental to solar water splitting efficiency, J. Mater. Chem. A 8 (2020) 20513, https://doi.org/10.1039/D0TA06524B.
[11] A.G. Tamirat, J. Rick, A.A. Dubale, W.-N. Su, B.-J. Hwang, Using hematite for photoelectrochemical water splitting: a review of current progress and challenges, Nanoscale Horiz. 1 (2016) 243, https://doi.org/10.1039/C5NH00098J.

[12] P.Y. Tang, J. Arbiol, Engineering surface states of hematite based photoanodes for boosting photoelectrochemical water splitting, Nanoscale Horiz. 4 (2019) 1256, https://doi.org/10.1039/C9NH00368A.
[13] R.V. De Krol, M. Gratzel. Photoelectrochemical Hydrogen Production, 1st ed., Springer, New York, 2012 https://doi.org/10.1007/978-1-4614-1380-6.
[14] E. Fabbri, A. Habereder, K. Waltar, R. Kötz, T.J. Schmidt, Developments and perspectives of oxide-based catalysts for the oxygen evolution reaction, Catal. Sci. Technol. 4 (2014) 3800, https://doi.org/10.1039/C4CY00669K.
[15] F. Song, M.M. Busch, B. Lassalle-Kaiser, C.S. Hsu, E. Petkucheva, M. Bensimon, H. M. Chen, C. Corminboeuf, X. Hu, An unconventional iron nickel catalyst for the oxygen evolution reaction, ACS Cent. Sci. 5 (2019) 558, https://doi.org/10.1021/acscentsci.9b00053.
[16] J. Song, C. Wei, Z.F. Huang, C. Liu, L. Zeng, X. Wang, Z.J. Xu, A review on fundamentals for designing oxygen evolution electrocatalysts, Chem. Soc. Rev. 49 (2020) 2196, https://doi.org/10.1039/C9CS00607A.
[17] M. Rioult, R. Belkhou, H. Magnan, D. Stanescu, S. Stanescu, F. Maccherozzi, C. Rountree, A. Barbier, Local electronic structure and photoelectrochemical activity of partial chemically etched Ti-doped hematite, Surf. Sci. 641 (2015) 310, https://doi.org/10.1016/j.susc.2015.01.002.
[18] H.C. Nguyën, F.A. Garcés-Pineda, M. De Fez-Febré, J.R. Galán-Mascarós, N. López, Non-redox doping boosts oxygen evolution electrocatalysis on hematite, Chem. Sci. 11 (2020) 2464, https://doi.org/10.1039/C9SC05669F.
[19] S. Stanescu, T. Alun, Y.J. Dappe, D. Ihiawakrim, O. Ersen, and D. Stanescu, Intrinsic photoanode band engineering: enhanced solar water splitting efficiency mediated by surface segregation in Ti-doped hematite nanorods. ChemRxiv. Cambridge: Cambridge Open Engage; 2023; This content is a preprint and has not been peer-reviewed. https://doi.org/10.26434/chemrxiv-2023-sxnbn.
[20] M. Rioult, D. Stanescu, E. Fonda, A. Barbier, H. Magnan, Oxygen vacancies engineering of iron oxides films for solar water splitting, J. Phys. Chem. C. 120 (2016) 7482, https://doi.org/10.1021/acs.jpcc.6b00552.
[21] B.S. Kalanoor, H. Seo, S.S. Kalanur, Recent developments in photoelectrochemical water-splitting using WO3/BiVO4 heterojunction photoanode: a review, Mater. Sci. Energy Technol. 1 (2018) 49, https://doi.org/10.1016/j.mset.2018.03.004.
[22] Z. Chen, T.F. Jaramillo, T.G. Deutsch, et al., Accelerating materials development for photoelectrochemical hydrogen production: Standards for methods, definitions, and reporting protocols, J. Mater. Res. 25 (2010) 3, https://doi.org/10.1557/JMR.2010.0020.
[23] J.A. Glasscock, P.R.F. Barnes, I.C. Plumb, N. Savvides, Enhancement of photoelectrochemical hydrogen production from hematite thin films by the introduction of Ti and Si, J. Phys. Chem. C. 111 (2007) 16477, https://doi.org/10.1021/jp074556l.
[24] C.X. Kronawitter, S.S. Mao, B.R. Antoun, Appl. Phys. Lett. 98 (2011), 092108, https://doi.org/10.1063/1.3552711.
[25] M.H. Lee, J.H. Park, H.S. Han, H.J. Song, I.S. Cho, J.H. Noh, K.S. Hong, Nanostructured Ti-doped hematite (α-Fe2O3) photoanodes for efficient photoelectrochemical water oxidation, Int. J. Hydrog. Energy 39 (2014) 17501, https://doi.org/10.1016/j.ijhydene.2013.10.031.
[26] L. Alibabaei, B.H. Farnum, B. Kalanyan, M.K. Brennaman, M.D. Losego, G. N. Parsons, T.J. Meyer, Atomic layer deposition of TiO2 on mesoporous nanoITO: conductive core–shell photoanodes for dye-sensitized solar cells, Nano Lett. 14 (2014) 3255, https://doi.org/10.1021/nl5006433.
[27] O. Zandi, B.M. Klahra, T.W. Hamann, Highly photoactive Ti-doped α-Fe2O3 thin film electrodes: resurrection of the dead layer, Energy Environ. Sci. 6 (2013) 634, https://doi.org/10.1039/C2EE23620F.
[28] F.F. Abdi, L. Han, A.H.M. Smets, M. Zeman, B. Dam, R. van de Krol, Efficient solar water splitting by enhanced charge separation in a bismuth vanadate-silicon tandem photoelectrode, Nat. Commun. 4 (2013) 2195, https://doi.org/10.1038/ncomms3195.
[29] A. Chemseddine, K. Ullrich, T. Mete, F.F. Abdia, R. van de Krol, Solution-processed multilayered BiVO4 photoanodes: influence of intermediate heat treatments on the photoactivity, J. Mater. Chem. A 4 (2016) 1723, https://doi.org/10.1039/C5TA08472E.
[30] L. Vayssieres, On the design of advanced metal oxide nanomaterials, Int. J. Nanotechnol. 1 (2004) 1, https://doi.org/10.1504/IJNT.2004.003728.
[31] C. Yilmaz, U. Unal, Single step synthesis of (α-Fe2O3) hematite films by hydrothermal electrochemical deposition, RSC Adv. 5 (2015) 16082, https://doi.org/10.1039/C4RA16028B.
[32] X. Lian, X. Yang, S. Liu, Y. Xu, C. Jiang, J. Chen, R. Wang, Enhanced photoelectrochemical performance of Ti-doped hematite thin films prepared by the sol–gel method, Appl. Surf. Sci. 258 (2012) 2307, https://doi.org/10.1016/j.apsusc.2011.10.001.
[33] H. Rarback, J.M. Kenney, J. Kirz, M.R. Howells, P. Chang, P.J. Coane, R. Feder, P.J. Houzego, D.P. Kern, and D. Sayre, Recent Results from the Stony Brook Scanning Microscope. In: Schmahl, G., Rudolph, D. (eds) X-Ray Microscopy, Springer Series in Optical Sciences, vol 43. Springer, Berlin, Heidelberg. https://doi.org/10.1007/978–3-540–38833-3_22.
[34] H. Ade, X. Zhang, S. Cameron, C. Costello, J. Kirz, S. Williams, Chemical contrast in X-ray microscopy and spatially resolved xanes spectroscopy of organic specimens, Science 258 (1992) 972, https://doi.org/10.1126/science.1439809.
[35] A.P. Hitchcock, Soft X-ray Imaging and Spectromicroscopy, Chapter 22 in Volume II (Methods) of the Handbook on Nanoscopy, eds. Gustaaf Van Tendeloo, Dirk Van Dyck and Stephen J. Pennycook (Wiley, 2012) 745–791. https://doi.org/10.1002/9783527641864.ch22.
[36] C.J. Jacobsen, X-ray Microscopy, Cambridge University Press, 2019, https://doi.org/10.1017/9781139924542.
[37] Joachim Stöhr, NEXAFS spectroscopy, Springer-Verlag Berlin Heidelberg, 1992, https://doi.org/10.1007/978-3-662-02853-7.
[38] F.M.F. de Groot, et al., 2p x-ray absorption spectroscopy of 3d transition metal systems, J. Electron Spectrosc. Relat. Phenom. 249 (2021), 147061, https://doi.org/10.1016/j.elspec.2021.147061.
[39] K.D. Malviya, H. Dotan, K.R. Yoon, I.-D. Kim, A. Rothschild, Rigorous substrate cleaning process for reproducible thin film hematite (α-Fe2O3) photoanodes, J. Mater. Res. 31 (2016) 1565, https://doi.org/10.1557/jmr.2015.300.
[40] M. Rioult, H. Magnan, D. Stanescu, A. Barbier, Single crystalline hematite films for solar water splitting: Ti-doping and thickness effects, J. Phys. Chem. C. 118 (2014) 3007–3014, https://doi.org/10.1021/jp500290j.
[41] B. Miao, A. Iqbal, K.H. Bevan, Utilizing band diagrams to interpret the photovoltage and photocurrent in photoanodes: a semiclassical device modeling study, J. Phys. Chem. C. 123 (2019) 28593, https://doi.org/10.1021/acs.jpcc.9b07536.
[42] B. Iandolo, B. Wickman, I. Zori, A. Hellman, The rise of hematite: origin and strategies to reduce the high onset potential for the oxygen evolution reaction, J. Mater. Chem. A 3 (2015) 16896, https://doi.org/10.1039/C5TA03362D.
[43] R. Belkhou, S. Stanescu, S. Swaraj, A. Besson, M. Ledoux, M. Hajlaoui, D. Dalle, HERMES: a soft X-ray beamline dedicated to X-ray microscopy, J. Synchrotron Radiat. 22 (4) (2015) 968, https://doi.org/10.1107/S1600577515007778.
[44] https://henke.lbl.gov/optical_constants/
[45] http://unicorn.chemistry.mcmaster.ca/axis/aXis2000-download.html
[46] https://spectromicroscopy.com/
[47] P. Quiteŕio, A. Apolinaŕio, D. Navas, S. Magalhaës, E. Alves, A. Mendes, C. Tavares Sousa, J. Pedro Araujo, Photoelectrochemical water splitting: thermal annealing challenges on hematite nanowires, J. Phys. Chem. C. 124 (2020) 12897, https://doi.org/10.1021/acs.jpcc.0c01259.
[48] V. Prabu, M. Obst, H. Hosseinkhannazer, M. Reynolds, S. Rosendahl, J. Wang, A. P. Hitchcock, Instrumentation for in-situ flow electrochemical scanning transmission x-ray microscopy (STXM), Rev. Sci. Instrum. 89 (2018), 063702, https://doi.org/10.1063/1.5023288.
[49] G. Righi, J. Plescher, F.-P. Schmidt, R.K. Campen, S. Fabris, A. Knop-Gericke, R. Schlögl, T.E. Jones, D. Teschner, S. Piccinin, On the origin of multihole oxygen evolution in haematite photoanodes, Nat. Catal. 5 (2022) 888, https://doi.org/10.1038/s41929-022-00845-9.